

# Effects of defect states on the performance of perovskite solar cells\*

Si Fengjuan(司凤娟), Tang Fuling(汤富领)<sup>†</sup>, Xue Hongtao(薛红涛), and Qi Rongfei(祁荣斐)

State Key Laboratory of Advanced Processing and Recycling of Non-ferrous Metals, Department of Materials Science and Engineering, Lanzhou University of Technology, Lanzhou 730050, China

**Abstract:** We built an ideal perovskite solar cell model and investigated the effects of defect states on the solar cell's performance. The verities of defect states with a different energy level in the band gap and those in the absorption layer  $\text{CH}_3\text{NH}_3\text{PbI}_3$  ( $\text{MAPbI}_3$ ), the interface between the buffer layer/ $\text{MAPbI}_3$ , and the interface between the hole transport material (HTM) and  $\text{MAPbI}_3$ , were studied. We have quantitatively analyzed these effects on perovskite solar cells' performance parameters. They are open-circuit voltage, short-circuit current, fill factor, and photoelectric conversion efficiency. We found that the performances of perovskite solar cells change worse with defect state density increasing, but when defect state density is lower than  $10^{16} \text{ cm}^{-3}$ , the effects are small. Defect states in the absorption layer have much larger effects than those in the adjacent interface layers. The perovskite solar cells have better performance as its working temperature is reduced. When the thickness of  $\text{MAPbI}_3$  is about  $0.3 \mu\text{m}$ , perovskite solar cells show better comprehensive performance, while the thickness  $0.05 \mu\text{m}$  for Spiro-OMeTAD is enough.

**Key words:** device modeling; defect states; perovskite solar cells

**DOI:** 10.1088/1674-4926/37/7/072003

**PACS:** 82.20.Wt; 88.40.H-; 78.56.-a

## 1. Introduction

Recently, hybrid organic–inorganic perovskites have become favorite solar cell materials owing to their outstanding semiconducting properties, such as high carrier mobility<sup>[1]</sup>, large absorption coefficient<sup>[2]</sup>, the direct band gap<sup>[3]</sup>, long charge-carrier diffusion lengths<sup>[4]</sup>, and multiple processing<sup>[5–9]</sup>. Over a short span of five years, a surprising conversion efficiency ( $E_{\text{ff}}$ ) has been achieved<sup>[10–13]</sup>. The  $0.1 \text{ cm}^2$  perovskites solar cells' certified efficiency was 17.8%<sup>[14]</sup>. In the laboratory the  $E_{\text{ff}}$  of small area devices has increased to nearly 20%<sup>[15, 16]</sup>. The  $E_{\text{ff}}$  of the module device can reach to 8.7%<sup>[17]</sup>, which is higher than a lot of other types of solar cells, and approach the level of commercial use. Therefore, perovskite solar cells are considered to be one of the most potential solar cells in the near future<sup>[18–20]</sup>. The overall performance of perovskite solar cells is improved with  $V_{\text{oc}}$  and  $J_{\text{sc}}$ 's increasing. The main reason is that this minimizes the interconnection losses of perovskite solar cells<sup>[21]</sup>. However, solar cell materials always have inevitable defect states, such as void, doping, surface or interface and so on, which always decrease solar cells'  $V_{\text{oc}}$  and  $J_{\text{sc}}$  then deteriorate the solar cells' performance<sup>[22–25]</sup>.

Some researchers had performed studies on defects' effects in perovskite solar cell materials. For example, Takashi Minemoto and Masashi Murata<sup>[26, 27]</sup> studied the impact of band offsets in perovskite solar cells with the one-dimensional device simulator SCAPS. Naikaew *et al.*<sup>[28]</sup> investigated the role of phase composition for electronic states in  $\text{MAPbI}_3$  prepared from a  $\text{CH}_3\text{NH}_3\text{I}/\text{PbCl}_2$  solution, and pointed out that a better understanding of defect formation and degradation is

crucial for successful development of stable solar cells. Rashkeev *et al.*<sup>[29]</sup> performed theoretical calculation on the characteristic of organometallic uniaxial ferroelectric semiconductor perovskite  $\text{MAPbI}_3$ , and point out that a lot of extended defects locate in organometallic solution-processed perovskite films, and these defects have high densities at domain walls and interfaces. Yin *et al.*<sup>[30]</sup> calculated the impacts of Cl and O at grain boundaries of  $\text{CH}_3\text{NH}_3\text{PbI}_3$ , and pointed out that the small Urbach tail<sup>[31]</sup> is in the sharp optical absorption edge introduced by the defect effects in the crystal.

In this paper, we analyze the impacts of defect states in the absorption layer and the adjacent interfaces on perovskite solar cells' performance<sup>[32]</sup>. With a similar modeling method, we had detected the defect effects in  $\text{CuInGaSe}_2$  solar cells<sup>[33]</sup>. Here we study the key feature parameters of perovskite solar cells with different energy level in the band gap and their defect states. Additionally, we also simulated the work temperature of perovskite solar cells and the thicknesses of absorber layer ( $\text{MAPbI}_3$ ) and hole transport material (Spiro-OMeTAD).

## 2. Theoretical model and device simulation parameters

We used the software SCAPS as the simulation platform<sup>[34]</sup>. In SCAPS we solve the Poisson equation and both continuity equations for electrons and holes iteratively. They are given respectively by Equations (1)–(7):

$$f_i(x) = \frac{c_n n(x) + e_p + e_p^{\text{opt}}(x)}{c_n n(x) + e_p + e_p^{\text{opt}}(x) + e_n + c_p p(x) + e_n^{\text{opt}}(x)}, \quad (1)$$

\* Project supported by the National Natural Science Foundation of China (Nos. 11164014, 11364025), the Gansu Science and Technology Pillar Program (No. 1204GKCA057), and the Gansu Supercomputer Center.

<sup>†</sup> Corresponding author. Email: tfl03@mails.tsinghua.edu.cn

Received 8 November 2015, revised manuscript received 30 December 2015

© 2016 Chinese Institute of Electronics

Table 1. Parameters of device simulation.

| Parameter                 | TCO       | Buffer    | IDL1            | Absorber             | IDL2            | HTM                  |
|---------------------------|-----------|-----------|-----------------|----------------------|-----------------|----------------------|
| Thickness (nm)            | 500       | 50        | 10              | 330                  | 10              | 350                  |
| $E_g$ (eV)                | 3.5       | 3.2       | 1.55 (variable) | 1.55 <sup>[1]</sup>  | 1.55 (variable) | 3.00 <sup>[36]</sup> |
| $N_t$ (cm <sup>-3</sup> ) | $10^{15}$ | $10^{15}$ | $10^{17}$       | $2.5 \times 10^{13}$ | $10^{17}$       | $10^{15}$            |

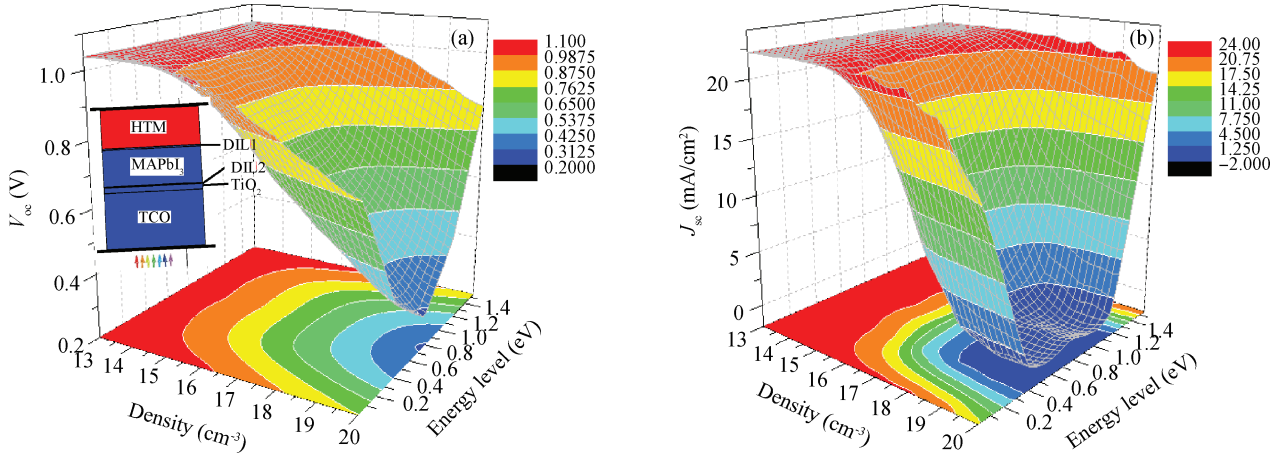


Figure 1. (Color online) The change of the (a)  $V_{oc}$  as well as (b)  $J_{sc}$  versus the defect state density in MAPbI<sub>3</sub>. The insert Figure 1(a) is the typical structure model of a perovskite solar cell.

$$\phi(\lambda, x) = \phi_{inc}(\lambda) f_c(\lambda, x) \exp \left[ - \int_0^x \alpha(\lambda, \xi) d\xi \right], \quad (2)$$

$$e_{n,p}^{opt}(x) = \int_{\lambda_1}^{\lambda_2} \sigma_{n,p}^{opt}(\lambda, x) \phi(\lambda, x) d\lambda, \quad (3)$$

$$\alpha(\lambda, x) = \alpha_{b-b}(\lambda) + \sum_{\forall \text{ defects}} \alpha_n(\lambda, x) + \alpha_p(\lambda, x), \quad (4)$$

$$\alpha_n(x, \lambda) = f_t(x) N_t(x) \sigma_n^{opt}(\lambda), \quad (5)$$

$$\alpha_p(x, \lambda) = [1 - f_t(x)] N_t(x) \sigma_p^{opt}(\lambda), \quad (6)$$

$$f_c(\lambda, x) = \frac{1 + R_b \exp \left[ -2 \int_x^L \alpha(\lambda, \xi) d\xi \right]}{1 - R_f R_b \exp \left[ -2 \int_0^L \alpha(\lambda, \xi) d\xi \right]}. \quad (7)$$

Here,  $f_t$  is the occupation probability of all defects,  $n$  and  $p$  are the electron and hole density respectively,  $c_n$ ,  $c_p$  are capture constants,  $e_n$ ,  $e_p$  are constants describing thermal emission from the trap centre,  $e_n^{opt}$ ,  $e_p^{opt}$  describe the optical emission,  $\phi_{inc}$  the incoming light flux and  $f_c$  an optical confinement factor. The absorption coefficient  $\alpha(\lambda, x)$  is the sum of all absorption processes that are considered. SCAPS considers the band to band absorption  $\alpha_{b-b}$  and absorption of the impurity photo-voltaic effect  $\alpha_n$  and  $\alpha_p$ ,  $R_b$  the reflection at the back and  $R_f$  the internal reflection at the front<sup>[35]</sup>.

In the device simulation, we considered a typical and ideal perovskite solar cell (inset of Figure 1(a)). The layered structure of the perovskite solar cell is: TCO (SnO<sub>2</sub>)/buffer (TiO<sub>2</sub>)/interface defect layer1 (IDL1)/absorber (MAPbI<sub>3</sub>)/interface defect layer2 (IDL2)/HTM (Spiro-OMeTAD). The parameters of TCO are from SnO<sub>2</sub>:F, the parameters of the buffer are from TiO<sub>2</sub>, the parameters of the absorber are from MAPbI<sub>3</sub>, and the parameters of HTM are

from 2,2',7,7'-tetrakis (N, N-p-dimethoxy-phenylamino)-9, 9'-spirobifluorene (Spiro-OMeTAD). There is an interface IDL1 between the buffer and absorber layers, and another interface IDL2 between the absorber and HTM layers. In order to explain this structure more clearly, Table 1 summarizes the input parameters for each layer. Here, the thicknesses of HTM and absorber were obtained from the literature: efficiency of the solar cell is 15.4%<sup>[6]</sup>,  $E_g$  is the band gap energy, and  $N_t$  is the defect density.

### 3. Results and discussion

As the perovskite absorption layer absorbs photons in the light, the photons whose energy are larger than the band gap of the absorption layer excite the valence band electron of the absorption layer to their conduction band, the appropriate hole stays in the valence band. When the conduction band energy level of the absorption layer is higher than that of the electron transport layer or the hole barrier layer, the conduction band electron of the absorption layer transfers to the conduction band energy level of the electron transport layer or the hole barrier layer. Finally, the electron transfers to the anode and external circuit<sup>[37]</sup>. If there are some unavoidable defects densities in the band gap of solar cell materials, they will affect the performance of the cell.

#### 3.1. Effects of the defect state to MAPbI<sub>3</sub>

Figures 1 and 2 show the effects of defect states to MAPbI<sub>3</sub>.

Theoretically, the locations of the density of defect states changes from the top of the valence band to the bottom of the conduction band. Figure 1(a) shows that the  $V_{oc}$  varies with the density of defect states in MAPbI<sub>3</sub>. From Figure 1(a), we can see that when the density of defect states in MAPbI<sub>3</sub> increases

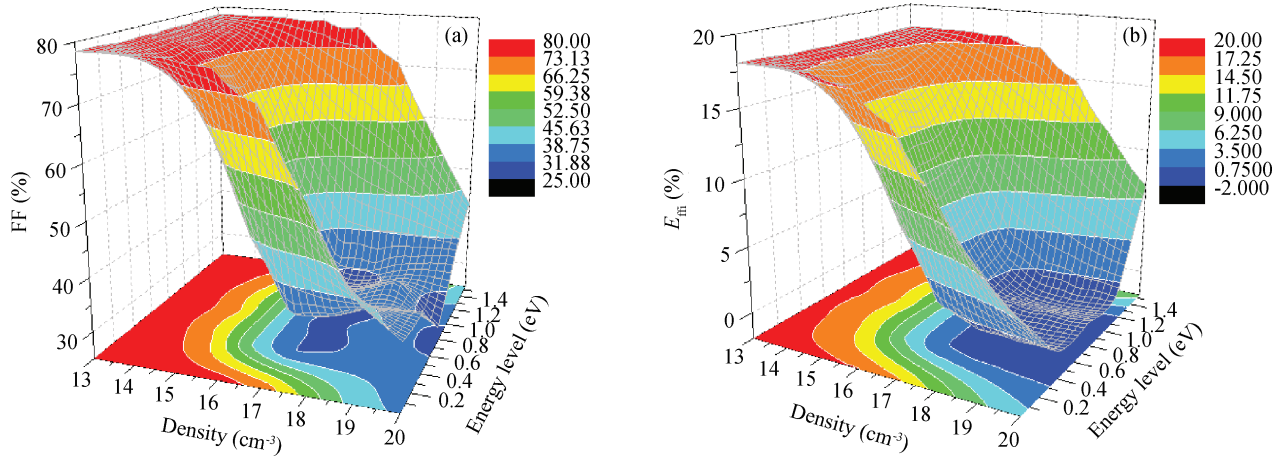


Figure 2. (Color online) The change of the (a) FF and (b)  $E_{fi}$  versus the defect state density in MAPbI<sub>3</sub>.

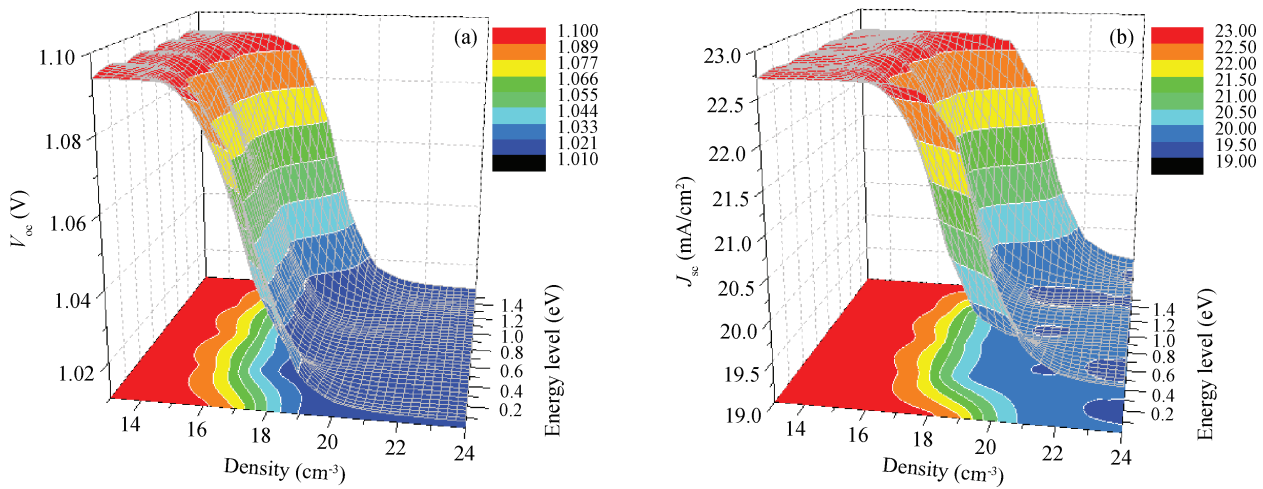


Figure 3. (Color online) The change of the (a)  $V_{oc}$  and (b)  $J_{sc}$  versus the defect state density in IDL1.

from  $2.5 \times 10^{13}$  to  $2.5 \times 10^{16} \text{ cm}^{-3}$ , the  $V_{oc}$  reduces from 1.038 to 0.814 V. In addition, when the density of defect states is lower than  $2.5 \times 10^{16} \text{ cm}^{-3}$ , the  $V_{oc}$  keeps smaller change at about 0.9 V, and the positions of the density of defect states have almost no effect on  $V_{oc}$ . Moreover, if the density of the defect state is larger than  $2.5 \times 10^{16} \text{ cm}^{-3}$ , the  $V_{oc}$  decreases to about 0.3 V, and the  $V_{oc}$  is not of practical application value.

Figure 1(b) shows the change of  $J_{sc}$  versus the density of defect states in MAPbI<sub>3</sub>. We find that the  $J_{sc}$  changes slightly from 17.27 to 22.17 mA/cm<sup>2</sup> as the density of the defect state is lower than  $2.5 \times 10^{16} \text{ cm}^{-3}$ . We also notice that once the density of the defect state is higher than  $2.5 \times 10^{16} \text{ cm}^{-3}$ , the  $J_{sc}$  falls quickly with the increasing of density of the defect state. From another aspect, we find that if the density of the defect state is higher than  $2.5 \times 10^{16} \text{ cm}^{-3}$ , the density of the defect state locates near the bottom of the conduction band or on the top of the valance band, the  $J_{sc}$  still keeps an ideal value near 20.0 mA/cm<sup>2</sup>.

Figures 2(a) and 2(b) show the change of the FF and  $E_{fi}$  versus the density of the defect state in MAPbI<sub>3</sub>. When the density of the defect state changes from  $2.5 \times 10^{16}$  to  $2.5 \times 10^{18} \text{ cm}^{-3}$  and near the middle of the band gap, the FF and  $E_{fi}$  decline from 78.38% to 30.35%, 17.94% to 0.07%, respectively. If defect states lie in the middle of the band gap instead of on

the bottom of the conduction band or at the top of the valence band, they have more bad impact on the properties of MAPbI<sub>3</sub> solar cells.

### 3.2. Effects of the defect state to IDL1 (buffer layer/MAPbI<sub>3</sub>)

We study the defect state's effects in the interface IDL1 (buffer layer/MAPbI<sub>3</sub>) and IDL2 (absorption layer/HTM). Figures 3 and 4 show the effects of the defect state in IDL1.

From Figure 3, we find that the  $V_{oc}$  is idealized and changes slightly around 1.09 V, where the defect state density is smaller than  $1.0 \times 10^{17} \text{ cm}^{-3}$ . We can see that the density of the defect state changes from  $1.0 \times 10^{17}$  to  $1.0 \times 10^{19} \text{ cm}^{-3}$ , the  $V_{oc}$  gradually decreases from 1.09 to 1.01 V. When the density of the defect state is up to  $1.0 \times 10^{19} \text{ cm}^{-3}$ ,  $V_{oc}$  is about 1.02 V. In addition, the  $V_{oc}$  changes slightly with the change of the location in band gap yet in short, the defect state in IDL1 always has a smaller effect on  $V_{oc}$ .

Figure 3(b) shows the change of the  $J_{sc}$ . In Figure 3(b), we can see that when the density of the defect state is less than  $1.0 \times 10^{17} \text{ cm}^{-3}$ , the defect state in IDL1 always has small effects on  $J_{sc}$  (it keeps stable about 22.7 mA/cm<sup>2</sup>). We also find that the  $J_{sc}$  decreases gradually from 22.7 to 20.0 mA/cm<sup>2</sup> as the

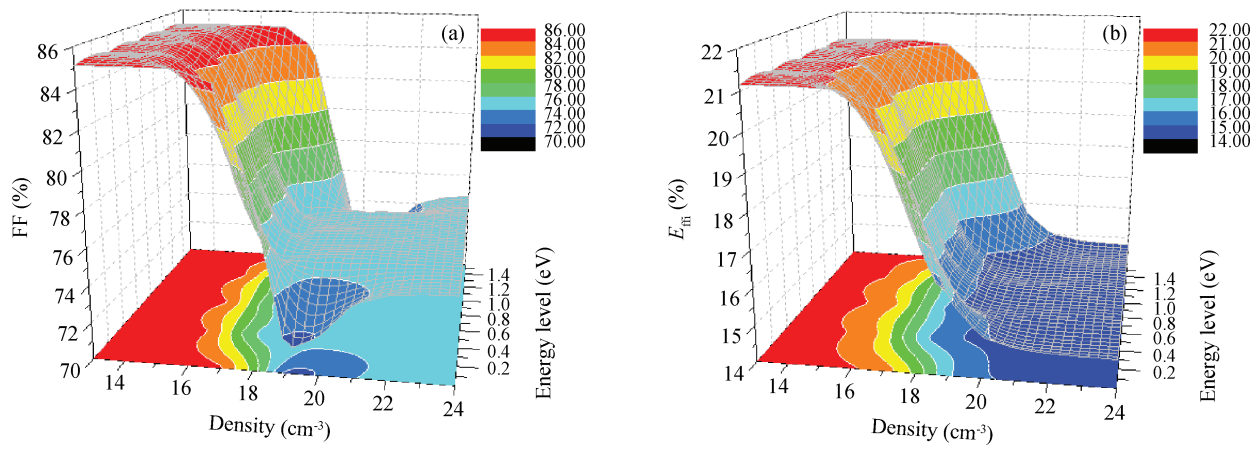


Figure 4. (Color online) The change of the (a) FF as well as (b)  $E_{ff}$  versus the defect state density in IDL1.

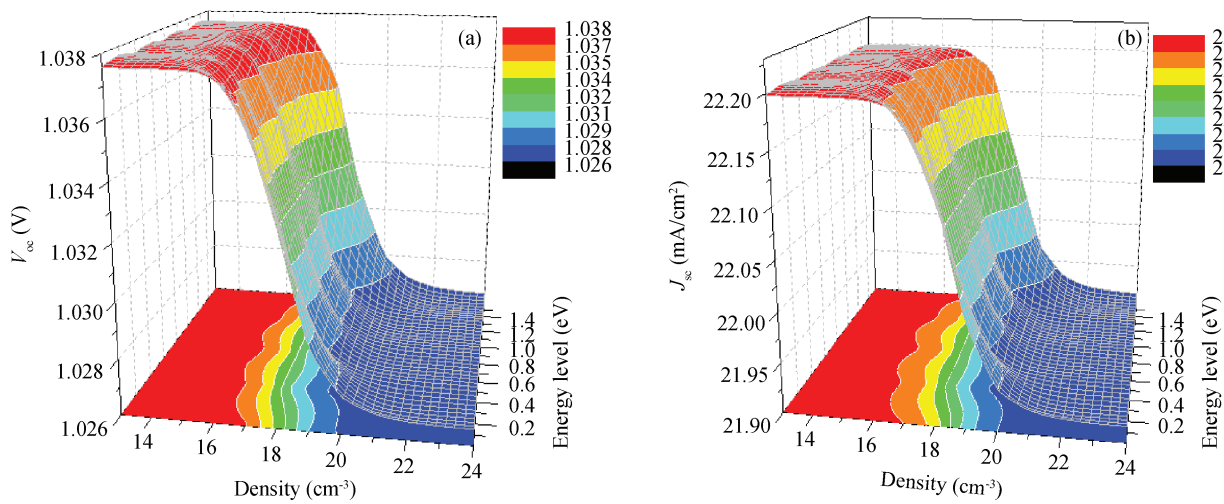


Figure 5. (Color online) The change of the (a)  $V_{oc}$  and (b)  $J_{sc}$  versus the defect state density in IDL2.

density of the defect state changes from  $1.0 \times 10^{17}$  to  $1.0 \times 10^{19} \text{ cm}^{-3}$ . We can consider that the  $J_{sc}$  slowly decreases as the location in the band gap changes between the top of the valance band and the bottom of the conductivity band.

Figure 4 shows the change of the FF and  $E_{ff}$ . From Figure 4(a), we can see that the FF has the maximum value of 85.1%, when the density of the defect state is less than  $1.0 \times 10^{16} \text{ cm}^{-3}$ . The  $E_{ff}$  also has its maximum value of 21.1%, while the density of the defect state is smaller than  $1.0 \times 10^{15} \text{ cm}^{-3}$ . From Figure 4(b), we can find that when the density of the defect state achieves the value of  $1.0 \times 10^{19} \text{ cm}^{-3}$ , the FF and  $E_{ff}$  are sensitive to the change of the defect state density. We also find that the FF decreases from 83% to around 70%, while  $E_{ff}$  decreases from 20% to around 14% when the density of the defect state is higher than  $1.0 \times 10^{17} \text{ cm}^{-3}$ .

### 3.3. Effects of the defect state to IDL2 (HTM/MAPbI<sub>3</sub>)

Effects of the defect state of IDL2 on  $V_{oc}$  and  $J_{sc}$  are shown in Figures 5(a) and 5(b). The  $V_{oc}$  is stable with the density of the defect state changing from  $1.0 \times 10^{13}$  to  $1.0 \times 10^{17} \text{ cm}^{-3}$ . When the density of the defect state is smaller than  $1.0 \times 10^{17} \text{ cm}^{-3}$ , the  $V_{oc}$  has its maximum value of 1.038 V, the  $J_{sc}$  also achieves its maximum value of 22.2 mA/cm<sup>2</sup>. When the den-

sity of the defect state is higher than  $1.0 \times 10^{17} \text{ cm}^{-3}$ , the  $V_{oc}$  changes from 1.037 to 1.027 V and  $J_{sc}$  changes from 22.20 to 21.92 mA/cm<sup>2</sup> slightly with the variation of the location in the band gap and the density of the defect state.

The changes of the FF (Figure 6(a)) as well as the  $E_{ff}$  (Figure 6(b)) are similar to that of the  $V_{oc}$  and  $J_{sc}$ . When the densities of the defect state are lower than  $1.0 \times 10^{17} \text{ cm}^{-3}$ , the FF changes around 78.1%, and the  $E_{ff}$  changes around 18.0%. When the densities of the defect state are higher than  $1.0 \times 10^{17} \text{ cm}^{-3}$ , the FF changes from 77.8% to 77.5%, while  $E_{ff}$  changes from 17.8% to around 17.4%. We note that the defect state in IDL2 also has smaller effects on  $V_{oc}$ ,  $J_{sc}$ , FF or  $E_{ff}$ .

### 3.4. The temperature's effects

The temperature ( $T$ ) effects are shown in Figure 7. The  $V_{oc}$  decreases linearly from 1.10 to 0.20 V with the increasing of the temperature from 270 to 700 K. As  $T$  changes from 270 to 700 K, the  $J_{sc}$  decreases from 22.2 to 21.2 mA/cm<sup>2</sup>, and it is not sensitive to  $T$ . FF gradually decreases as  $T$  increases from 270 to 700 K. The change of  $E_{ff}$  is similar to that of the  $V_{oc}$ ,  $E_{ff}$  also decreases linearly with the increasing of the temperature from 270 to 700 K. According to our results, perovskite solar cells have a better performance when they work at lower



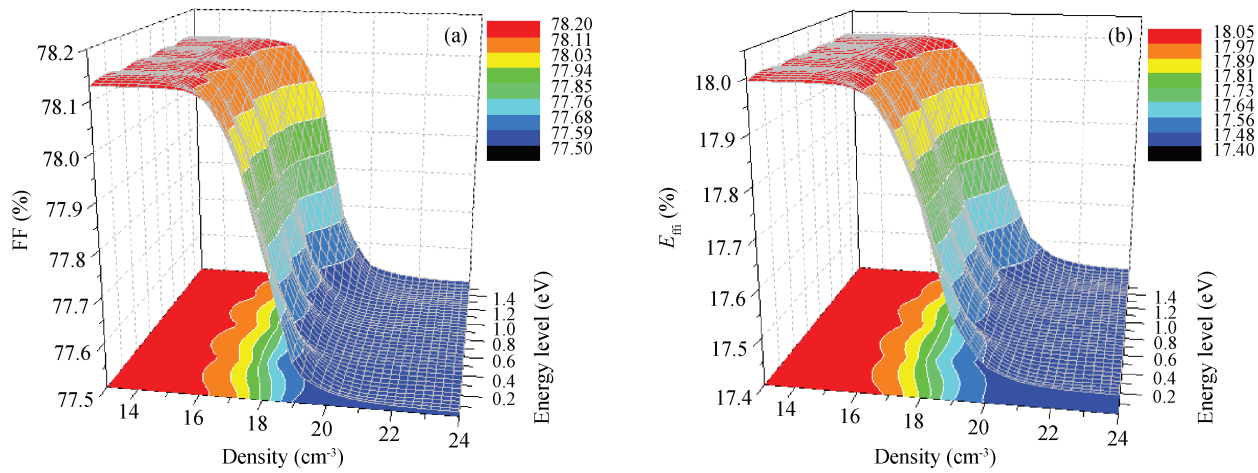


Figure 6. (Color online) The change of the (a) FF as well as (b)  $E_{ff}$  versus the defect state density in IDL2.

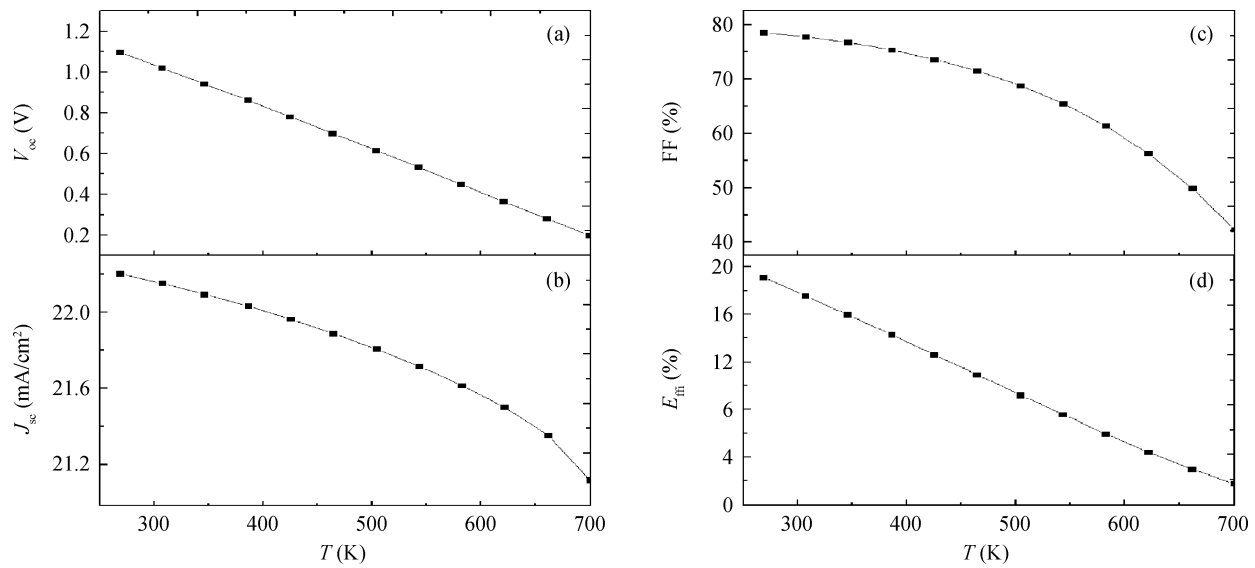


Figure 7. The change of the (a)  $V_{oc}$ , (b)  $J_{sc}$ , (c) FF as well as (d)  $E_{ff}$  versus temperature ( $T$ ).

temperature.

### 3.5. Effects of the thickness (absorption layer and hole transport layer)

Figures 8 and 9 indicate that influences of thickness of MAPbI<sub>3</sub> absorption layer and that of Spiro-OMeTAD hole transport layer, respectively.

In Figure 8(a), as the thickness of MAPbI<sub>3</sub> increases from 0.05 to 0.264  $\mu\text{m}$ , the  $V_{oc}$  gradually increases from 0.91 to 1.031 V. The  $V_{oc}$  gradually increases from 1.031 to 1.037 V as the thickness of MAPbI<sub>3</sub> increases from 0.264 to 0.8  $\mu\text{m}$  and the thickness of Spiro-OMeTAD is 0.46  $\mu\text{m}$ . However, the thickness of Spiro-OMeTAD has almost no influence on the  $V_{oc}$ . In Figure 8(b), the thicknesses of MAPbI<sub>3</sub> and Spiro-OMeTAD have larger effects on  $J_{sc}$  than those on  $V_{oc}$ . As the thickness of MAPbI<sub>3</sub> increases from 0.05 to 0.264  $\mu\text{m}$ ,  $J_{sc}$  increases sharply from 9.99 to 21.00 mA/cm<sup>2</sup>. When the thickness of MAPbI<sub>3</sub> increases from 0.264 to 0.8  $\mu\text{m}$ ,  $J_{sc}$  gradually increases from 21.00 to 24.03 mA/cm<sup>2</sup>. The thickness of Spiro-OMeTAD also has almost no influence on  $V_{oc}$  and  $J_{sc}$ .

In Figure 9(a), as the thickness of MAPbI<sub>3</sub> increases from 0.05 to 0.3  $\mu\text{m}$ , and when the thickness of Spiro-OMeTAD is less than 0.3  $\mu\text{m}$ , FF has a maximum value of about 81%. As the thicknesses of MAPbI<sub>3</sub> and Spiro-OMeTAD increase, the FF gradually decreases.  $E_{ff}$  variation trends are similar to that of  $V_{oc}$ : as the thickness of MAPbI<sub>3</sub> increases from 0.05 to 0.22  $\mu\text{m}$ ,  $E_{ff}$  increases from 7.13% to 17.31% (Figure 9(b)). As the thickness of MAPbI<sub>3</sub> increases from 0.3 to 0.8  $\mu\text{m}$ ,  $E_{ff}$  keeps almost stable. It is worth pointing out that compared with the change of the  $V_{oc}$ ,  $E_{ff}$  is sensitive to the change of the thickness of MAPbI<sub>3</sub>. Our results indicate that the performance of perovskite solar cells is little influenced by the thickness of Spiro-OMeTAD. Because the preparation process of Spiro-OMeTAD is very complex, and its price is five times that of gold, so we use the least amount possible in designing the perovskite solar cells.

## 4. Conclusion

We built an ideal perovskite solar cell, and carried out a theoretical research on the effects of defect states (energy

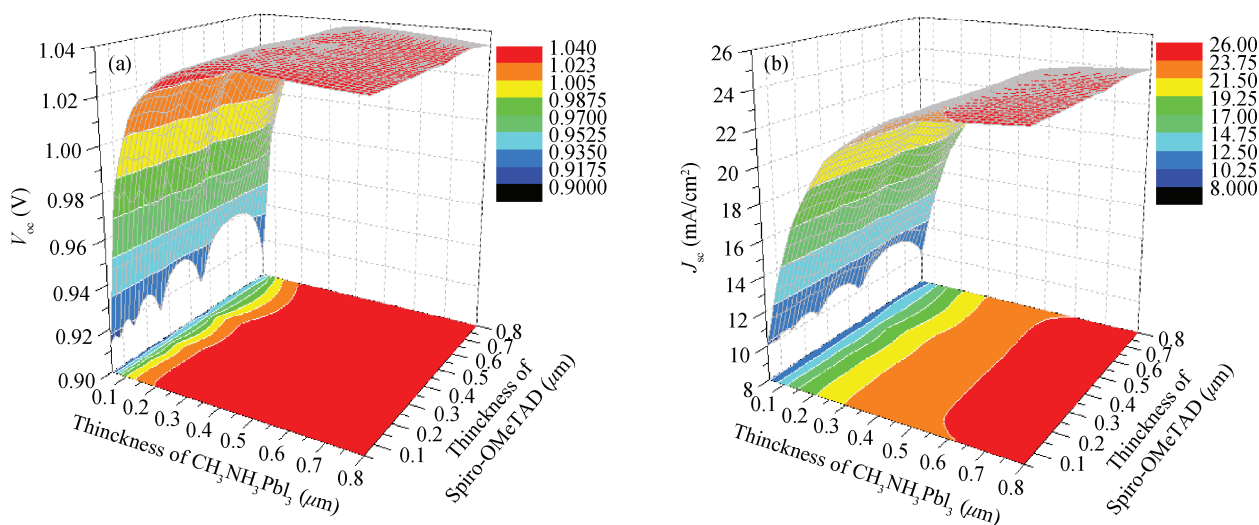


Figure 8. (Color online) The change of the (a)  $V_{oc}$  and (b)  $J_{sc}$  versus the thickness of MAPbI<sub>3</sub> and Spiro-OMeTAD layers.

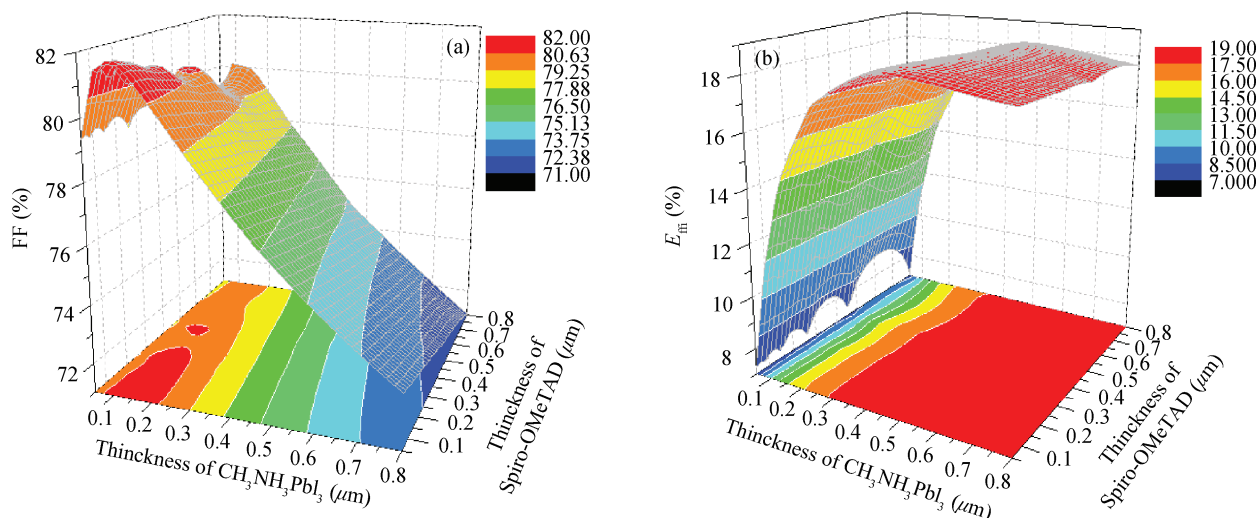


Figure 9. (Color online) The change of the (a) FF and (b)  $E_{ff}$  versus the thickness of MAPbI<sub>3</sub> and Spiro-OMeTAD layers.

level in band gap and defect state densities in absorption layer MAPbI<sub>3</sub>, and that in buffer layer/absorbing layer interface as well as in absorption layer/hole layer interface) to its performance. The main results: (1) the defect states have a large effect on the performance of perovskite solar cells when the defect state density is higher than  $10^{16} \text{ cm}^{-3}$ , while defect states have a small effect when the defect state density is lower than  $10^{16} \text{ cm}^{-3}$ ; (2) defect states in the absorption layer have a much larger effect than those in the adjacent interface layers; (3) the perovskite solar cells have better performance as its working temperature is reduced; and (4) when the thickness of MAPbI<sub>3</sub> is about  $0.3 \mu\text{m}$ , the properties of perovskite solar cells are better, and the thickness  $0.05 \mu\text{m}$  of Spiro-OMeTAD is enough.

## References

- [1] Noh J H, Im S H, Heo J H, et al. Chemical management for colorful, efficient, and stable inorganic–organic hybrid nanostructured solar cells. *Nano Lett*, 2013, 13: 1764
- [2] Stoumpos C C, Malliakas C D, Kanatzidis M G. Semiconducting tin and lead iodide perovskites with organic cations: phase transitions, high mobilities, and near-infrared photoluminescent properties. *Inorganic Chemistry*, 2013, 52: 9019
- [3] Stranks S D, Eperon G E, Grancini G, et al. Electron-hole diffusion lengths exceeding 1 micrometer in an organometal trihalide perovskite absorber. *Science*, 2013, 342: 341
- [4] Xing G, Mathews N, Sun S, et al. Long-range balanced electron- and hole-transport lengths in organic–inorganic  $\text{CH}_3\text{NH}_3\text{PbI}_3$ . *Science*, 2013, 342: 344
- [5] Ball J M, Lee M M, Hey A, et al. Low-temperature processed meso-superstructured thin-film perovskite solar cells. *Energy Environmental Science*, 2013, 6: 1739
- [6] Liu M, Johnston M B, Snaith H J. Efficient planar heterojunction perovskite solar cells by vapour deposition. *Nature*, 2013, 501: 395
- [7] Chen Q, Zhou H, Hong Z, et al. Planar heterojunction perovskite solar cells via vapor-assisted solution process. *Journal of the American Chemical Society*, 2014, 136: 622
- [8] Burschka J, Pellet N, Moon S J, et al. Sequential deposition as a route to high-performance perovskite-sensitized solar cells. *Nature*, 2013, 499: 316
- [9] Xue Q F, Sun C, Hu Z C, et al. Recent advances in perovskite solar cells: morphology control and interfacial engineering. *Acta*

- Chimica Sinica, 2015, 73: 179
- [10] Wang Q, Shao Y C, Dong Q F, et al. Large fill-factor bilayer iodine perovskite solar cells fabricated by a low-temperature solution-process. *Energy Environmental Science*, 2014, 10: 2359
- [11] Hodes G. Perovskite-based solar cells. *Science*, 2013, 342: 317
- [12] Abrusci A, Stranks S D, Docampo P, et al. High-performance perovskite-polymer hybrid solar cells via electronic coupling with fullerene monolayers. *Nano Lett*, 2013, 13: 3124
- [13] Liu M Z, Johnston M B, Snaith H J. Efficient planar heterojunction perovskite solar cells by vapour deposition. *Nature*, 2013, 501: 395
- [14] Nakayashiki S, Daisuke H, Ogomi Y, et al. Interface structure between titania and perovskite materials observed by quartz crystal microbalance system. *Journal of Photonics for Energy*, 2015, 5: 057410
- [15] Zhou H P, Chen Q, Li G, et al. Interface engineering of highly efficient perovskite solar cells. *Science*, 2014, 345: 542
- [16] Dai Xiaoyan, Shi Chengwu, Zhang Yanru, et al. Hydrolysis preparation of the compact TiO<sub>2</sub> layer using metastable TiCl<sub>4</sub> isopropanol/water solution for inorganic-organic hybrid heterojunction perovskite solar cells. *Journal of Semiconductors*, 2015, 36: 074003
- [17] Seo J, Park S, Kim Y C, et al. Benefits of very thin PCBM and Li F layers for solution-processed p-i-n perovskite solar cells. *Energy Environmental Science*, 2014, 7: 2642
- [18] Wang Duofa, Tao Haizheng, Zhao Xiujian, et al. Enhanced photovoltaic performance in TiO<sub>2</sub>/P3HT hybrid solar cell by interface modification. *Journal of Semiconductors*, 2015, 36: 023006
- [19] Bouhdjar A F, Ayat L, Meftah A M, et al. Computer modeling and analysis of the photodegradation effect in a-Si:H p-i-n solar cell. *Journal of Semiconductors*, 2015, 36: 014002
- [20] Liu Jian, Huang Shihua, He Lu. Simulation of a high-efficiency silicon-based heterojunction solar cell. *Journal of Semiconductors*, 2015, 36: 044010
- [21] Song J, Li S S, Huang C H, et al. Device modeling and simulation of the performance of Cu(In<sub>1-x</sub>Ga<sub>x</sub>)Se<sub>2</sub> solar cells. *Solid-State Electron*, 2004, 48: 73
- [22] Lin Aiguo, Ding Jianning, Yuan Ningyi, et al. Analysis of the p+/p window layer of thin film solar cells by simulation. *Journal of Semiconductors*, 2012, 33: 023002
- [23] Datta A, Damon-Lacoste J, Cabarrocas P R, et al. Defect states on the surfaces of a P-type c-Si wafer and how they control the performance of a double heterojunction solar cell. *Solar Energy Materials and Solar Cells*, 2008, 92: 150015
- [24] Xu Z T, Mitzi D B. SnI<sub>4</sub>-based hybrid perovskites templated by multiple organic cations combining organic functionalities through noncovalent interactions. *Chemistry of Materials*, 2003, 15: 3632
- [25] Wang Jianqiang, Gao Hua, Zhang Jian, et al. Investigation of an a-Si/c-Si interface on a c-Si(P) substrate by simulation. *Journal of Semiconductors*, 2012, 33: 033001
- [26] Datta A, Damon-Lacoste J, Nath M, et al. Dominant role of interfaces in solar cells with N-a-Si: H/P-c-Si heterojunction with intrinsic thin layer. *Mater Sci Eng B*, 2009, 159: 10
- [27] Minemoto T, Murata M. Theoretical analysis on effect of band offsets in perovskite solar cells. *Solar Energy Materials and Solar Cells*, 2015, 133: 8
- [28] Naikaew A, Prajongtat P, Lux-Steiner M C, et al. Role of phase composition for electronic states in CH<sub>3</sub>NH<sub>3</sub>PbI<sub>3</sub> prepared from CH<sub>3</sub>NH<sub>3</sub>I/PbCl<sub>2</sub> solution. *Appl Phys Lett*, 2015, 106: 23210
- [29] Rashkeev S N, El-Mellouhi F, Kais S, et al. Domain walls conductivity in hybrid organometallic perovskites: The key of CH<sub>3</sub>NH<sub>3</sub>PbI<sub>3</sub> solar cell high performance. *Scientific Reports*, 2015, 5: 11467
- [30] Yin W J, Chen H Y, Shi T T, et al. Origin of high electronic quality in structurally disordered CH<sub>3</sub>NH<sub>3</sub>PbI<sub>3</sub> and the passivation effect of Cl and O at grain boundaries. *Adv Electron Mater*, 2015, 1: 1500044
- [31] Wolf C D, Holovsky J, Moon S J, et al. Organometallic Halide Perovskites: sharp optical absorption edge and its relation to photovoltaic performance. *Phys Chem Lett*, 2014, 5: 1035
- [32] Nollet P, Kontges M, Burgelman M, et al. Indications for presence and importance of interface states in CdTe/CdS solar cells. *Thin Solid Films*, 2003, 431/432: 414
- [33] Wan Fucheng, Tang Fuling, Xue Hongtao, et al. Effects of defect states on the performance of CuInGaSe<sub>2</sub> solar cells. *Journal of Semiconductors*, 2014, 35: 024011
- [34] Verschraegen J, Khelifi S, Burgelman M, et al. Numerical modeling of the impurity photovoltaic effect (IPV) in SCAPS. 21st European Photovoltaic Solar Energy Conference, 2006: 396
- [35] Burgelman M, Nollet P, Degraeve S. Modeling polycrystalline semiconductor solar cells. *Thin Solid Films*, 2000, 361-362: 527
- [36] Poplavskyy D, Nelson J. Nondispersive hole transport in amorphous film of methoxy-spirofluorene-arylamine organic compound. *J Appl Phys*, 2003, 93: 341
- [37] Wang J T W, Ball J M, Barea E M, et al. Low-temperature processed electron collection layers of graphene/TiO<sub>2</sub> nanocomposites in thin film perovskite solar cells. *Nano Lett*, 2014, 14: 724